A generalized CSA-ODF model for Fiber Orientation Mapping

A THESIS
SUBMITTED TO THE FACULTY OF THE GRADUATE SCHOOL
OF THE UNIVERSITY OF MINNESOTA
BY

Amith J. Kamath

IN PARTIAL FULFILLMENT OF THE REQUIREMENTS
FOR THE DEGREE OF
MASTER OF SCIENCE

Advisors:
Prof. Christophe Lenglet and Prof. Tryphon Georgiou

September, 2012

Acknowledgements

I wish to extend my gratitude to my advisors, Prof. Christophe Lenglet and Prof. Tryphon Georgiou for having faith in me to work on Diffusion Image analysis. It has been my privilege to work in a field encompassing all these exciting areas: Signal Processing, Medical Image analysis, Machine Learning and Brain Anatomy. I am indebted to them for all the guidance and support extended throughout the past year.

I would also like to thank Prof. Guillermo Sapiro for having instilled in me a sense of awe at research in Image Processing and the importance of mathematics in all walks of life. The two courses I had the opportunity to sit through under him were possibly the best I've ever had. Thank you so much for all your support and encouragement.

This is a great opportunity to thank Dr. Iman Aganj, who has been more than a mentor and guide in helping me understand his work, without which there wouldn't be any algorithm to generalize. His prompt responses to my emails, and clear understanding of problems I faced made my research move over many hurdles. I would also like to thank Dr. Julio Duarte for all his support in making my code work much faster than I could ever hope.

I would like to thank Prof. Mihailo Jovanovic for accepting my request to be part of the defense jury and showing some interest in my research problem.

Finally, no amount of gratitude can represent the support and love I have received from my family back in India, and friends here in Minnesota and I hope they will be proud of my work!

Dedication

To the brave: who tread the path less taken;
To those who believe the answer to everything lies in data;

Abstract

This work involves advances in modeling and estimating white matter fiber orientations for use in tractography studies and axonal microstructure analysis in the human brain. We make use of preferential movement of water along axon fibers rather than across it's membrane as an indirect measure using MRI data acquisition sensitized to diffusion. Over the past decade, several mathematically elegant models have been proposed, with varying acceptance levels from the clinical fraternity. With practical feasibility in mind, the trade-offs between resolution, acquisition time and SNR make the optimization of data capture protocols ever more crucial. We focus on generalizing the current state-of-art models to allow for any acquisition scheme, and go on to understand how the acquisition parameters affect the results.

The Constant Solid Angle -Orientation Distribution Function (CSA-ODF) model provides a vital correction in the Q-ball method for High Angular Resolution Diffusion Imaging (HARDI) data. The HARDI data is decomposed on a modified Spherical Harmonic (SH) basis, due to which the otherwise necessary 3-D inverse Fourier Transform can be easily estimated using a linear approximation of the Funk Radon Transform (FRT) on a single shell. This results in a simple linear-least-squares approximation, prone to over-fitting errors and low SNR. We explore an adaptive regularization scheme to generalize well for the inverse problem of interpolating the q-space data. We use a bi-exponential radial signal decay model, which uses more information about the axonal microstructure than the single-shell approximation. The 'staggered' acquisition scheme increases the angular spread of samples and allows for higher angular resolution of the fiber orientations.

A comprehensive analysis of the reconstruction is shown on synthetic data, and the best parameters for acquisition is demonstrated. The optimal level of b-value, number of gradient directions, order of SH decomposition and interpolation is derived from experiments, and results on a brain data set is shown to validate the method. We hope that this generalization of the CSA-ODF algorithm is going to provide better models of the diffusion process in MR images, and prove to be a guide for setting up the acquisition protocols for the Human Connectome Project and other future studies.

Contents

List of Tables

List of Figures

Chapter 1

Introduction

" The way Calvin's brain is wired, you can almost hear the fuses blowing."
- Bill Watterson, the Complete Calvin and Hobbes.

In the past decade, there have been unprecedented developments in understanding how the human brain works [1, 2]. New tools have been developed to characterize the functions and structure of the brain. The neuro-imaging community is evolving rapidly, and has benefitted greatly from advances in nuclear physics, machine learning, signal processing and high-performance computing. The ability to peer into a live, functioning human body to detect anomalies and fix it non-invasively has been the holy grail for healthcare. With the advent of X-ray scans and it's generalization into tomographic reconstructions, MRI and PET scans, carrying out accurate diagnosis has come to depend quite heavily on these technologies.

MR Imaging is by far the most promising imaging modality for both anatomic and functional imaging. It is based on the principle of Nuclear Magnetic Resonance (NMR) [3]. In the 50's, NMR evolved to allow for measuring spatial characteristics of matter, with Herman Carr measuring the first 1-D NMR signal. Paul Lauterbur came up with methods to do this in 2-D and 3-D, and so the first NMR image was taken in 1973. Realizing that the inclusion of 'Nuclear' in the terminology has it's negative connotations, the technology would simply be called Magnetic Resonance (MR), and subsequently MR Imaging (MRI) in the 2-D and 3-D case. Soon afterwards in 1974,

the first in-vivo MR image of mouse was published. The MR Image found great clinical use in distinguishing pathological tissue from normal tissue. Brain Tumors showed up with a different intensity than surrounding tissues, and the rest as they say is history.

1.1 The Human Brain

The human Brain has long been considered one of the most complicated research subject. It is especially exciting as it's study is recursive, in that understanding the brain depends on complexity of the brain itself. It is the sole organ responsible for rendering the sense of existence to other parts of the body. As Dr. V. S. Ramachandran elaborates in his book, 'Phantoms of the Brain', it is vested with powers to make the real feel like imaginary, and the imaginary feel like real [4]. Weighing at around 3 lbs, the complexity of axonal fibers has fascinated anatomists from times immemorial. It is estimated that there is more than 150,000 km of myelinated axons [5] in a volume less than 1500 cm^3. Figure 1.1 shows the complexity of the fiber structure.

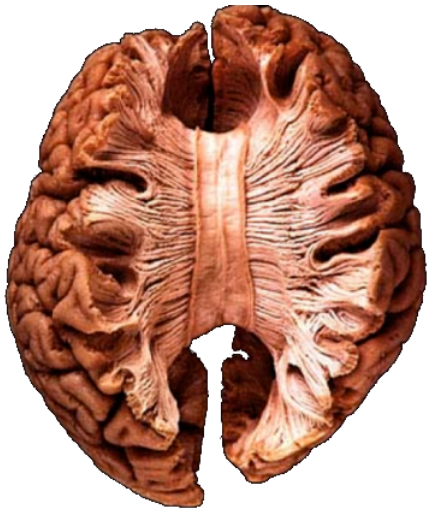

Figure 1.1: White matter structure of the brain: complex interconnect of fibers.

The human brain can be broadly classified into regions called gray and white matter. White matter, long thought to be passive tissue, actively affects how the brain learns and dysfunctions. Grey matter is primarily associated with processing and understanding, whereas white matter acts as a relay and coordinates communication between different

brain regions. White matter is composed of bundles of axons, which is a long slender cylindrical appendage that transmits signals away from the Neuron cell body. Information processing happens in the gray matter, and the white matter functions as a network-interconnect for these computing clusters located in the periphery of the brain cortex. As Sebastian Seung points out in 'I am my connectome', every person is endowed with a unique neural circuitry. This is what makes us: us [6]. MR Images have added a new dimension to our understanding of the brain, and it's inner working. This has been further developed by the discovery of being able to measure water diffusion which can provide information about the anatomical microstructure in the brain.

1.2 Magnetic Resonance Imaging

NMR uses the property of magnetic spin, inherent to atoms with an odd number of protons or neutrons. These atoms have a magnetic moment which will resonate with an external magnetic field. The hydrogen ion has this property, and tends to align with the applied field to maintain a low energy configuration. This state can be perturbed with application of Radio frequency waves which add energy into the rotating system. The RF energy needs to be at a specific frequency defined by the Magnetic Field strength at that location. Like in the case of a spinning top in a gravitational field, the proton tends to precess around the applied field direction. The essential requirement of MR acquisition is to localize the excitation and response of this signal so as to estimate spatial properties of the medium. The process of exciting the protons using RF signals is typically represented by a pulse sequence. In Figure 1.2, the magnetization vector is represented by $\vec{M}$, and its components along the z-axis and in the orthogonal x-y plane are shown.

The process of MR image acquisition in a nutshell is as follows. A strong uniform magnetic field, typically 1.5 T and above is applied throughout the volume to be imaged. This sets up the alignment of protons in the direction along the field. Once the system reaches this low energy state, RF pulses are applied, which perturbs the spin of the protons to be in the orthogonal plane. Once the RF pulse ceases to exist, the protons precess around the main field, and tend to reach the equilibrium state through an exponential recovery process. Local variations in the main field strength, quantum

effects, variations in composition and density of protons affect the recovery rate. These variations characterize the tissue type in that region, and hence shows up as different intensities in the MR image. This is generally called a T1 weighted image, where T1 represents the time constant for the signal recovery along the main field. Fluids like water have a T1 of $1500 - 2000$ ms. This is illustrated in the Figure 1.3. If TR is the time allowed for recovery, the signal measured should have a characteristic:

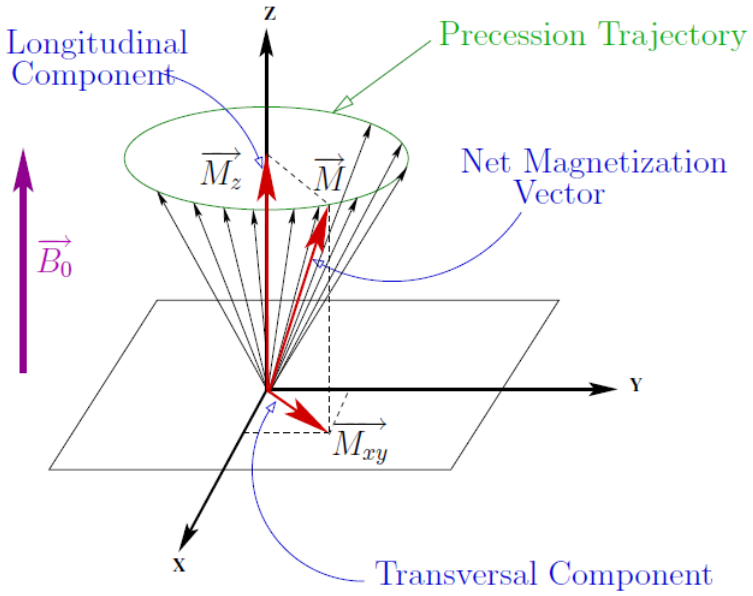

Figure 1.2: Magnetization vector and its components.

$$S = M_0(1 - e^{\frac{-TR}{T1}}) \tag{1.1}$$

T2 relaxation is the mechanism with which the transverse component of the magnetization decays, and is usually much faster than T1. T2 scans are called 'pathology scans' as they show good contrast against abnormal tissues. Since T2 is faster and harder to detect, a pulse sequence protocol called spin-echo has been developed. This relies on including a 180 degree pulse in between the 90 degree pulses so as to reverse the order of dephasing. This will bring all the precessing magnetizations in phase after a fixed time period. Due to local inhomogeneities, the rephasing is not perfect. This becomes an indirect measurement of local tissue properties. If T1 effects are ignored,

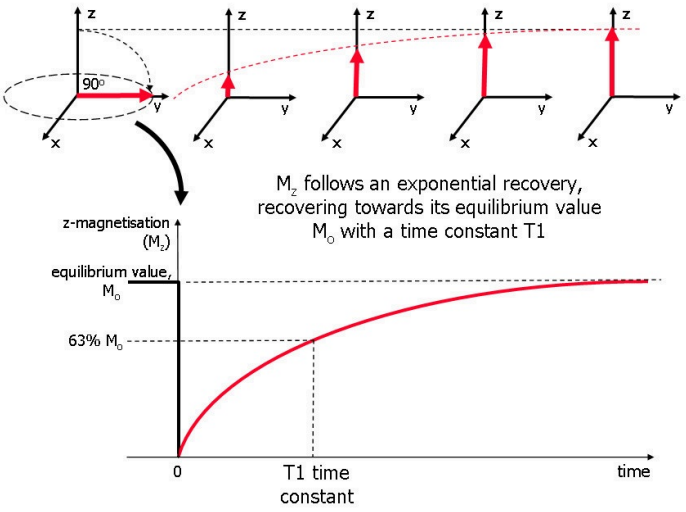

Figure 1.3: T1 recovery process

and TE is the time at which the signal is measured, then

$$S = M_0 e^{\frac{-TE}{T2}} \tag{1.2}$$

would be the expression relating the signal to T2. The T2 decay is illustrated in Figure 1.4.

Diffusion MR imaging is based on T2 scans with added diffusion magnetic gradients. These gradient fields are applied along a particular direction, and are typically represented as $\mathbf{G}$. Depending on the orientation of the field $\mathbf{G}$, a measure of the magnitude of water diffusion along that direction is estimated, giving a sense of fiber structure. The duration between the two diffusion gradient pulses called Δ determines the time allowed for the protons to diffuse. With longer diffusion times, the dependence on direction becomes stronger, with the trade-off of having a lower SNR. The effect of varying pulse sequence characteristics and gradient strength is embedded into a single parameter called the b-value. Higher b-value indicates greater diffusion time, and lower SNR.

MR Imaging would not be possible without some intelligent signal processing methods for spatial localization. CT scans use a shadow based tomographic reconstruction

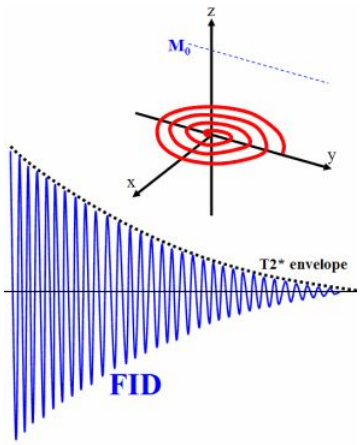

Figure 1.4: T2 decay and precession

techniques, so that multiple 1-D projections can be combined to produce a 2-D representation of the internal structure. MR Imaging uses frequency selection for choosing a small 3-D region in space, generally in the range of $2x2x2$ cubic mm and lower. Each 2-D slice in the object can be excited separately using a specific RF signal. This relates distance to a spatial frequency which needs to be inverse fourier transformed. When extrapolated to 3D, this becomes computationally expensive. One of the driving factors for optimizing MR scans is acquisition time, which needs to be minimal especially in cases of non-compliance. The trade-off here is between better image resolution and shorter acquisition time.

1.3 The Research Problem

Over the past decade, newer geometric models for Diffusion data have driven faster acquisition protocols. Since 1994 when Peter Basser at NIH introduced the Diffusion Tensor model [7], several mathematically elegant formulations have been devised. DTI allowed new findings in fiber tractography, and eventually studies regarding the entire human connectome. In 2004, David Tuch at MIT proposed the Q-ball imaging technique [8] which made better fiber orientation resolutions practical. In 2007, Descoteaux et al. used spherical harmonic bases to make the computations involved in Q-ball imaging easier [9]. Advances in MR hardware also helped decrease signal acquisition time. In

2010, Aganj et al. corrected mathematical inaccuracies in the Q-ball model for achieving sharper fiber orientation estimates [10].

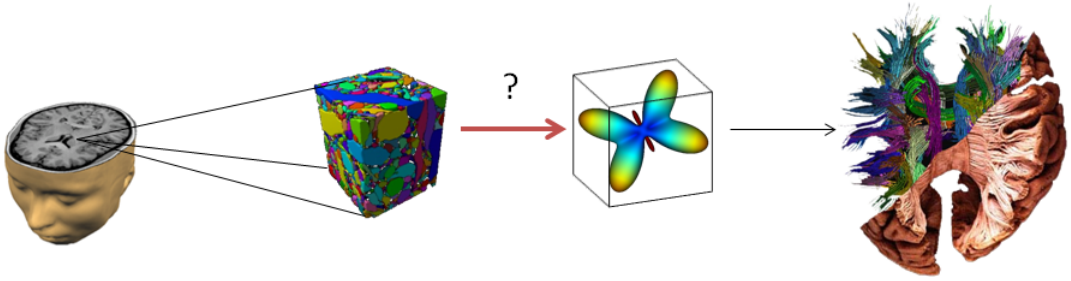

Figure 1.5: The Diffusion MR Imaging problem: an illustration

As Fig. 1.5 shows, the motivation behind this thesis is to optimize the step indicated by the red-arrow. This happens to be a critical pre-processing stage for tractography studies which will lead to a better understanding of the human connectome, unlocking information about several brain-related conditions. This work relates to generalizing this model, called Constant-Solid-Angle Orientation Distribution Function (CSA-ODF) to support *any* acquisition scheme. We use a bi-exponential signal approximation to better fit the data, and follow it up with a comprehensive analysis of optimizing the acquisition parameters based on well known synthetic data models. We propose an acquisition scheme that makes the most out of the controllable parameters to improve reconstruction accuracies, and present our results on human brain data.

1.4 Outline

The rest of this thesis is organized as follows. We begin with Chapter 2 on Methods, where an introduction on Diffusion Imaging algorithms is presented. A brief section on the Diffusion Tensor model is next. This is followed by a section on Q-ball Imaging, one of the basic HARDI reconstruction techniques. The CSA-ODF algorithm is then elaborated with special emphasis on computational aspects. This chapter ends with a discussion on regularization, which turns out to be a crucial factor in the algorithm.

The results are presented in Chapter 3, including preliminary discussion on the experimentation process. Results for optimization of b-value follows, which is used in the

next step of choosing the minimum number of gradient directions to reduce acquisition time. The algorithm needs quality checks, with respect to orientation accuracy measures, and a short discussion on this follows. Finally, results on a human brain data are presented, along with some explanation on the interpretation.

This is followed by Chapter 4, summarizing the contributions and including future directions for research.

Chapter 2

Methods

" temet nosce - know thyself. " - popularized by the Wachowski brothers in the Matrix.

2.1 Preliminaries

Diffusion effects have been explained since the 1800's when Robert Brown studied random movements of pollen grains through his microscope. In the early part of the 20th century, Albert Einstein, in the quest for proof of existence of atoms came up with a probabilistic framework to describe the ensemble motion of particles undergoing diffusion. Now called 'Brownian Motion', this is an inherent property of all fluids above absolute 0, and results in particle mixing without there being a bulk transport phenomenon. Einstein in 1905 introduced the 'displacement distribution', which relates the mean-squared displacement of the ensemble, with a quantity called 'diffusion coefficient': D, for a given diffusion time Δ, as shown in Eq. 2.1. In a free medium like in a glass of water away from the boundary, this diffusion can be approximated as a Gaussian process, defined entirely by D.

$$\langle x^2 \rangle = 2D\Delta \tag{2.1}$$

The dependence of diffusion on geometric structures can be used as an indirect measure of non-invasively detecting the structure. We will quickly describe the physics behind MR scans and follow it up with the modeling algorithms.

2.1.1 MR Physics

NMR is a phenomenon where particles with a magnetic spin when placed in a magnetic field absorb and re-emit radiation. This frequency specifically depends on the strength of the applied magnetic field. When a person enters a MR scanner, his body is subject to a strong magnetic field, typically 1.5 T and above. The coordinate axis is set so that the main field points to the z-axis. At these field strengths, the radiation is at around 64 MHz, in the RF range. The RF pulse, called the 90 degree pulse flips the magnetization from the z-axis to the x-y plane. As is the property of any spinning body in a force field, the particle starts precessing: a phenomenon called Larmor precession, as represented in figure 2.1. The angular frequency of this precession is governed by the Larmor Equation 2.2.

$$\omega = \gamma B \tag{2.2}$$

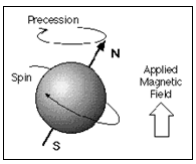

Figure 2.1: A proton precessing in a magnetic field.

where B is the magnetic field strength, and γ is called the gyromagnetic ratio, approximately equal to $2.68 * 10^8$ rad/s/T for the proton. This precessing magnetization decays transversely, and slowly reaches the low energy state when it is along the main field. This process is at a particle level. At current levels of resolution (which depends on the main field strength) of 2 x 2 x 2 cubic mm, millions of protons exist. The signal that we detect is thus an aggregate signal from all protons in that volume. All the protons do not precess with exactly the same frequency, due to local inhomogeneities in the field and material coomposition differences. The signal thus dephases and reaches equilibrium at slightly different decay rates. This is efficiently captured via the 'spin-echo' experiment.

2.1.2 The spin-echo experiment

In 1950, Edwin Hahn proposed a method to effectively capture this decay using an ingenious setup. If a 180 degree pulse is applied when the particles are precessing, it will reverse their phases, meaning that particles spinning faster will have a phase lag, and slower spins will have an equivalent phase lead. Eventually, after the same time gap between the time when the precessing began in-phase and the phase reversal, all the particles will return to be in-phase, which is when the signal decay can be captured. This is represented in figure 2.2 and in case of diffusion imaging, is called the Stejskal Tanner Pulse Gradient Spin Echo (PGSE) sequence [11].

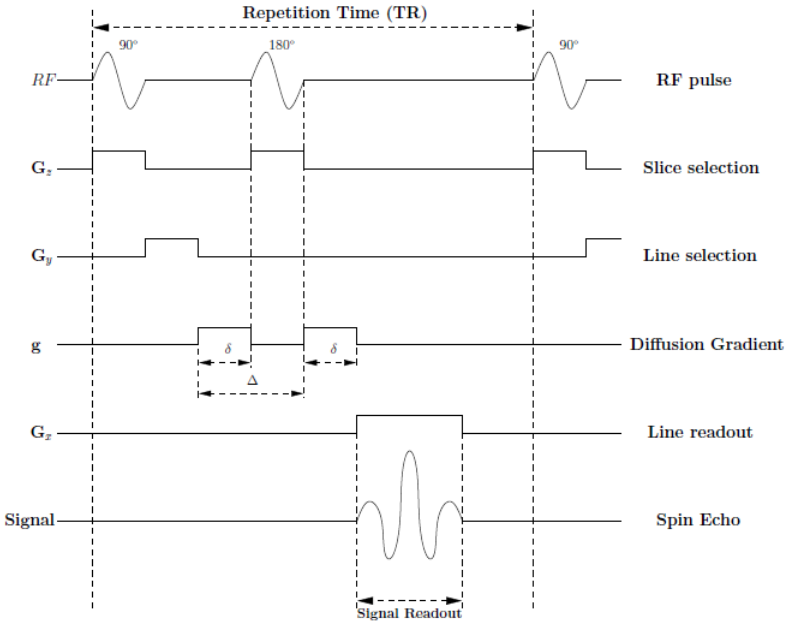

Figure 2.2: Stejskal Tanner PGSE Pulse sequence.

In 1954, Carr and Purcell used Hahn's spin-echo experiment to sensitize the MR signal to proton diffusion. In addition to the main magnetic field, they added a 'magnetic field gradient' which induced different precessional frequencies based on the location of the proton. The phase shifts change with time too, and this can be measured as before. The amount of phase change points to the rate of diffusion. In 1965, Stejskal and Tanner introduced the Pulsed-Gradient-Spin-Echo (PGSE) scheme which clearly distinguishes

the encoding stage (pulse duration δ) from the decoding stage (after Δ). All these parameters are grouped into a single quantity called 'b-value', which is proportional to the square of the applied field. The expression for b-value is

$$b = \gamma^2 g^2 \delta^2 (\Delta - \frac{\delta}{3}) \tag{2.3}$$

and this is one of the parameters we will tune for obtaining sharp fiber orientation features.

2.1.3 *Q*-space

Diffusion MR signals are measured in q-space, which happens to be in the 3-D spatial frequency domain. This is due to the application of magnetic field gradients and frequency based image encoding techniques. A slice is selected from the volume by including a z-axis gradient, which linearly varies the Larmor frequency required for excitation. RF pulses of a given frequency thus excites just one slice and tips the magnetization vector in that 2-D region. In the selected slice, gradients are applied along the in-plane directions, in the x-y plane.This linear variation in field induces a linear variation in the Larmor frequency. Each proton thus gets a spin phase change θ based on it's location (x, y) as

$$\theta = 2\pi((\gamma \int G_x(t)dt)x) + (\gamma \int G_y(t)dt)y)) \tag{2.4}$$

where G_x and G_y are the strengths of the applied gradients at (x,y). The signal thus received in the coil can be represented using the fourier relation

$$s(t) = \int f(x, y) e^{i2\pi\theta} dxdy \tag{2.5}$$

where *f(x,y)* is the MR signal that has to be retrieved. This needs to be done using the inverse Fourier Transform. The equivalent spatial frequency space is called the 'k-space' which can be sampled during the experiment by changing the gradient amplitude and slew rate. The rules of Nyquist sampling apply here in 2-D and hence the image resolution can be tuned as required. Typically, if higher main field strengths are used, resolution can be improved.

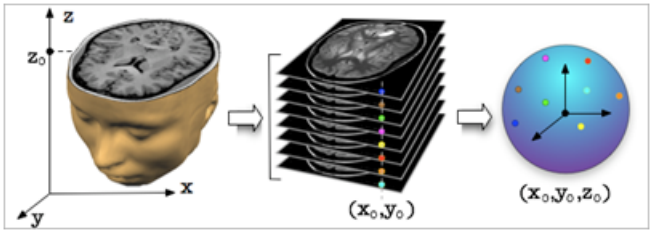

Figure 2.3: Q-space represented by the blue sphere (right), each point of which generates a complete volume.

The concept of q-space in diffusion imaging is analogous to k-space. A 3-D space inside of each voxel is defined by the vector q which is sampled with each PGSE acquisition.With repeated acquisitions, varying in direction and gradient strength, points in this 3-D space can be sampled. This is represented pictorially in Fig. 2.3, where each point on the blue sphere corresponds to a single acquisition, and many such acquisitions lead to multiple images of the same slice, with measurements on different directions.

This has to be inverse fourier transformed in 3-D to obtain the spatial displacement distribution. This forms the basis for Diffusion Spectrum Imaging (DSI), where nyquist sampling of the displacement distribution in q-space is carried out to obtain a complete model-free profile for diffusion.

2.1.4 Diffusion Equations

Due to the T1 recovery and T2 relaxation processes in the precession, the MR signal at any particular location (x, y, z) in a slice could be represented as

$$S_0(x, y, z) = M_0(1 - e^{\frac{-TR}{T1}})e^{\frac{-TE}{T2}} \tag{2.6}$$

where TR is called the repetition time, the time allowed for recovery along the main field, and TE is called the Echo time, at which the spin-echo occurs. Due to the addition of diffusion gradients, the MR signal is sensitized to particle motion as well. This adds another exponential decay term into the equation, as

$$S_D(x, y, z) = M_0(1 - e^{\frac{-TR}{T1}})e^{\frac{-TE}{T2}}e^{-bD} \tag{2.7}$$

where b is the b-value used during acquisition, and D is the Apparent Diffusion

Coefficient (ADC). b encodes the magnitude and direction along which the acquisition is made, and hence defines samples in the q-space.

Equation 2.6 can be thought of as an acquisition where $b = 0$. This when used as a normalization for the $b \neq 0$ images helps in the estimation of D as

$$D(x, y, z) = \frac{log(\frac{S_0(x,y,z)}{S_D(x,y,z)})}{b} \tag{2.8}$$

This assigns a scalar measure $D(x, y, z)$ for each voxel and is sufficient if the diffusion is isotropic. This formulation is sufficient for gray matter voxels, which contain cell structures that are not tubular.

2.2 Diffusion Tensor Imaging

Early research into modeling the ADC began with the Diffusion Tensor model. In the isotropic case, a scalar measure of the ADC is sufficient for representation of the diffusion profile. This can be represented as a sphere of radius D, the scalar value. In case of white matter voxels, it is known that the ADC is directionally dependent. This calls for using 3-D geometric representations of the displacement distribution profile. A simple generalization of the sphere is an ellipsoid, which the DTI model employs.

2.2.1 Formulation

Introduced in 1994 by Peter Basser, DTI aims at modeling this 3-D diffusion profile as an ellipsoid [7]. The length of the semi-major axis and it's orientation specifies the approximate direction of the fibers in that particular voxel. Along with the $b = 0$ image, a minimum of 6 samples need to be taken in distinct directions in q-space for reconstruction. The ADC, (D) has been modeled as a $3x3$ symmetric positive definite matrix, commonly used to represent tensors.

$$D = \begin{bmatrix} D_{xx} & D_{xy} & D_{xz} \\ D_{yx} & D_{yy} & D_{yz} \\ D_{zx} & D_{zy} & D_{zz} \end{bmatrix} \tag{2.9}$$

It is safe to assume that diffusion processes are radially symmetric, and hence $D_{ij} = D_{ji}$ for all *i,j*. This becomes a 3-D covariance matrix, where the diagonal elements correspond to diffusivities along the coordinate axes. This also induces zero-mean Gaussianity to the process, as it could be represented as

$$S(g) = S_0 e^{-bg^T Dg} \tag{2.10}$$

where $S(g)$ is the diffusion weighted signal with gradient vector g and S_0 is the unweighted signal. This tensor defines an ellipsoid, with it's eigenvectors pointing to the axes, and corresponding eigenvalues measuring it's length. The largest eigenvalue and it's eigenvector completely determine the direction of the fiber estimated in that voxel. When all the three off-diagonal elements are zero, the ellipsoid is aligned with the coordinate axes. An illustration of the different ellipsoids is shown in Figure **??**.

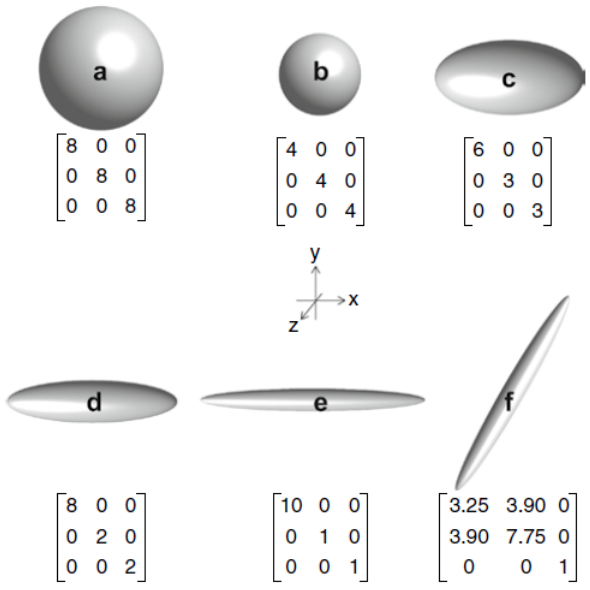

Figure 2.4: Ellipsoid shapes and the corresponding D tensor.

If the eigenvalues are denoted by λ_1, λ_2 and λ_3, and the corresponding eigenvectors by e_1, e_2 and e_3, the orientation of the tensor is taken to be parallel to the principal eigenvector e_1 and the diffusivity is measured by λ_1, the largest eigenvalue. If $\lambda_2 = \lambda_3$, the shape becomes cylindrically symmetric around the principal eigenvector, and it is

usually called a zeppelin.

2.2.2 Computational Issues

Several computationally efficient methods for estimation of D have been proposed. The simplest of them is the Ordinary Least Squares (OLS) method, which relies on a gaussian noise approximation. Due to the need for estimating 6 parameters, 6 independent sample directions are sufficient. Let us assume that N independent samples in q-space are acquired [2]. This amounts to estimating D from a system of N linear equations. This is represented as follows:

$$ln(\frac{S(g)}{S_0}) = -bg^T Dg \tag{2.11}$$

$$ln(\frac{S(g)}{S_0}) = -b_{xx}D_{xx} - b_{yy}D_{yy} - b_{zz}D_{zz} - 2b_{xy}D_{xy} - 2b_{yz}D_{yz} - 2b_{xz}D_{xz}. \tag{2.12}$$

If $ln(\frac{S(g)}{S_0})$ is represented as a column matrix $\mathbf{S}$ and $\mathbf{B}$ is a N x 6 matrix encoding the gradient table information and $\mathbf{D}$ is the vector containing the elements of D unrolled, then

$$\mathbf{S} = \mathbf{BD} \tag{2.13}$$

and with an ordinary least squares inversion,

$$\mathbf{D} = (\mathbf{B^T B})^{-1}\mathbf{B^T S} \tag{2.14}$$

Non-linear regression methods especially the Levenberg-Marquardt Algorithm have also been used for estimating D.

2.2.3 Anisotropy Measures

Quantifying the sharpness (anisotropy) for fiber estimates is essential for post-processing and visualizing the data. With the tensor scheme, several such measures have been used.

One such measure is called Fractional Anisotropy (FA) and is represented as

$$FA = \sqrt{\frac{3}{2}} \frac{\sqrt{(\lambda_1 - \hat{\lambda})^2 + (\lambda_2 - \hat{\lambda})^2 + (\lambda_3 - \hat{\lambda})^2}}{\sqrt{\lambda_1^2 + \lambda_2^2 + \lambda_3^2}} \tag{2.15}$$

where $\hat{\lambda}$ is the trace of the eigenvalues,

$$\hat{\lambda} = \frac{(\lambda_1 + \lambda_2 + \lambda_3)}{3} \tag{2.16}$$

In regions like the corpus callosum, the fiber tracts are uniformly aligned, and hence the diffusivity as measured in a voxel will have a strong directionality. The FA in these regions will be nearly equal to 1, as compared to regions in the gray matter where it will be close to 0.

The Mean Diffusivity ($\hat{\lambda}$) image is also used for a high-level understanding of the diffusion processes in the brain. With ever more complex models being used currently, scalar measures like these are used often to validate the reconstruction with known anatomical structures.

2.2.4 Drawbacks

With current levels of spatial resolution of a voxel, it is estimated that 1/3 of all voxels in the brain contain more than one principal fiber orientation [12]. The tensor model assumes a single fiber, and hence fails to accurately reconstruct these voxels. Further studies have revealed complex fiber structures, including fanning, kissing and diverging fibers which can be approximated with gross errors in a DTI setting. With a fixed model complexity, no room is allowed for adapting the reconstruction technique to the data. Models like the Multi-Tensor, which estimates two separate ellipsoids have been published, but they too are not sufficient for modeling complex diffusion profile shapes. This is one of the reasons why tractography studies based on DTI were not hugely popular amongst clinicians. The following sections address these drawbacks, and attempt to define a more descriptive model for multiple fiber configurations in the brain.

2.3 Q-ball Imaging: CSA-ODF Algorithm

With the knowledge that a single fiber approximation is not sufficient for accurate tractography studies, and advances in signal acquisition techniques that allos more points to be sampled in q-space, model-free techniques like Diffusion Spectrum Imaging (DSI) [13] and Q-Ball imaging came to be popular [8]. Q-ball imaging aims at estimating the linear radial projection of the displacement distribution, which is a real function on the unit sphere.

2.3.1 Formulation

We denote by $P(\vec{r})$ the 3-D probability distribution of water diffusion. This quantifies the probability that a proton initially at the origin is located at an infinitesimal volume dv located at $\vec{r}$ after a certain amount of time, defined by TE. By symmetry, $P(-\vec{r}) = P(\vec{(r)})$ and it is usually represented using spherical coordinates (r, θ, ϕ). With this formulation, the volume element dv can be written as $r^2 dr d\Omega$, with $d\Omega = sin(\theta) d\theta d\phi$, the infinitesimal solid angle element. Rather than actually measuring this PDF, it is desirable to measure it's dependence on just (θ, ϕ) by radial integration. This quantity is called the Orientation Distribution Function (ODF). If $\hat{u}$ denotes the unit vector along r, then

$$ODF(\hat{u}) = \int_{r=0}^{r=\infty} P(r\hat{u}) r^2 dr \tag{2.17}$$

This quantity is a function of (θ, ϕ) and measures the marginal probability that the proton diffuses along that direction, irrespective of the distance $|r|$. We desire to calculate this ODF from $E(\vec{q})$, samples of the 3-D fourier transform of the PDF $P(\vec{(r)})$. To do so, some basic properties of the 3-D fourier transform are used in simplifying the computation, effectively making this problem solvable via a linear matrix operation.

2.3.2 Computational Issues

Calculating the ODF involves the computation of the 3-D fourier inverse, which has an unfavorable time complexity. Several methods including using intelligent signal basis functions, dictionary-based methods have been developed to make this more tractable.

We focus on an algorithm based on work by Descoteaux et al. [**?**], where spherical harmonic series are used to decompose real functions on the sphere. The advantage of using this specific basis is that they are eigenfunctions of the Laplace-Beltrami operator (∇_b^2), which renders the Funk-Radon Transform (FRT) computation trivial. We begin by listing some basic properties used in this process.

Preliminaries

From fourier analysis, we relate the laplacian of the 3-D fourier transform of a function as

$$F\{|\vec{r}|^2 P(\vec{r})\} = -\nabla^2 E(\vec{q}). \tag{2.18}$$

Also, for a symmetric function $P : \Re^3 :\rightarrow \Re$ with the 3-D fourier transform $E(\vec{q})$,

$$\int_0^\infty P(r\hat{u})dr = \frac{1}{8\pi^2}\int\int_{\hat{u}^\perp} E(\vec{q})d^2q \tag{2.19}$$

where $u^\perp$ defines the orthogonal plane for a given $\hat{u}$. This leads to the relation

$$ODF(\hat{u}) = -\frac{1}{8\pi^2}\int\int_{\hat{u}^\perp} \nabla^2 E(\vec{q})d^2\vec{q} \tag{2.20}$$

The Laplacian in this equation when represented in the spherical co-ordinates neatly decomposes to a radial term and the Laplace-Beltrami operator. The radial term (∇_q^2, dependent on q only) turns out to be a constant.

$$\nabla_q^2 E(\vec{q}) = \frac{1}{q}\frac{\partial^2}{\partial q^2}(qE) \tag{2.21}$$

$$\int^{2\pi}\int_0^\infty \frac{1}{q}\frac{\partial^2}{\partial q^2}(qE)qdqd\phi = -2\pi \tag{2.22}$$

The Laplace-Beltrami term remains to be solved, and is calculated using the Funk-Radon Transform. The Laplace-Beltrami operator turns out to be a measure of smoothness of functions on the sphere, and this property is going to be used in the regularization process.

$$\nabla_b^2 E(\vec{q}) = \frac{1}{sin(\theta)}\frac{\partial}{\partial\theta}(sin(\theta)\frac{\partial E}{\partial\theta}) + \frac{1}{sin^2(\theta)}\frac{\partial^2 E}{\partial\phi^2} \tag{2.23}$$

The equation for calculating the ODF thus simplifies to

$$ODF(\hat{u}) = \frac{1}{4\pi} - \frac{1}{8\pi^2}\int_0^{\infty}\int_0^{2\pi}\frac{1}{q}\nabla_b^2 E(\vec{q})d\phi dq \tag{2.24}$$

which is equivalent to

$$ODF(\hat{u}) = \frac{1}{4\pi} - \frac{1}{8\pi^2}\int_0^{\infty} FRT\{\frac{1}{q}\nabla_b^2 E(\vec{q})\}dq \tag{2.25}$$

Funk-Radon Transform

The Funk-Radon Transform (FRT) maps functions of the sphere to itself. The FRT of a spherical function E at a point $\hat{u}$ on the sphere is the integral of E over the great circle $G(\hat{u})$ which lies in the plane perpendicular to $\hat{u}$ through the origin. This is represented in the Fig. 2.5, where it can be observed that the signal value along the axis is high due to the high values on the orthogonal plane. The signal levels in the orthogonal plane happens to be low because the integral in it's orthogonal plane has a lower value. The samples acquired on the q-ball of a particular radius as specified by the b-value is used in this estimation. The FRT assumes a continuous representation of the function E on the sphere, and hence the samples need to be interpolated. The FRT is mathematically defined as

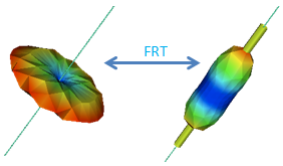

Figure 2.5: The Funk Radon Transform for a single fiber configuration.

$$FRT\{E(\vec{q})\} = \int_{\hat{u}^{\perp}} E(\vec{q})dq \tag{2.26}$$

Signal Modeling

This formulation still requires the radial integral, which assumes the knowledge of signal levels at al $|q|$ for a given direction $\hat{u}$. An exponential decay model is used to simplify

this. It has been shown in prior studies that the q-space signal decays exponentially, as defined by

$$E(q\hat{u}) \approx e^{-\alpha q^2} \tag{2.27}$$

where α is calculated knowing the signal sample on the shell with radius q_0, and that the signal has to equal 1 at the origin. $E(0)$ is the zero-frequency signal, and the equality with 1 is essential for the ODF to actually be a probability density function. Assuming this model, the expression for ODF reduces to

$$ODF(\hat{u}) = \frac{1}{4\pi} - \frac{1}{8\pi^2} FRT\{\nabla_b^2 ln(-ln(E(\vec{q})))\} \tag{2.28}$$

These signal measurements are noisy, and since this system has equal number of equations and unknowns, it demands regularization. We shall delve into the signal representation issues in the next few sections, where advances in this domain is discussed.

Spherical Harmonics Basis

Spherical Harmonics (SH): shown in Fig. 2.6, are typically denoted by Y_l^m with l specifying the order and m, the phase factor. They are a basis for functions on the unit sphere. They are calculated at (θ, ϕ) as

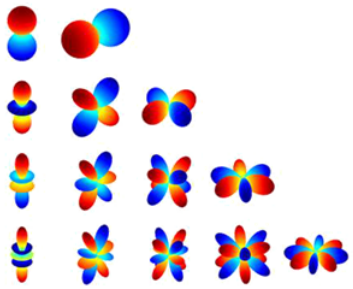

Figure 2.6: Spherical Harmonics: Even order: 2, 4, 6, 8.

$$Y_l^m(\theta, \phi) = \sqrt{\frac{2l+1}{4\pi} \frac{(l-m)!}{(l+m)!}} P_l^m(cos(\theta)) e^{im\phi} \tag{2.29}$$

where P_l^m is the associated legendre polynomial. To make use of the symmetry of $P(\vec{r})$, we use only even orders of SH series so that odd (anti-symmetric) basis functions

are eliminated. Hence for $l = 0, 2, 4, ..., l_{max}$ and $m = -l, ..., 0, ..., l$ we define $j = j(l, m) = (l^2 + l + 2)/2 + m$ and use this new basis

$$Y_j = \begin{cases} \frac{1}{\sqrt{2}}((-1)^m Y_l^m + Y_l^{-m}), & \text{if } -l \leq m < 0 \\ Y_1^0, & \text{if } m = 0 \\ \frac{1}{\sqrt{2}}((-1)^m Y_l^m + Y_l^{-m}), & \text{if } -l \leq m < 0 \end{cases} \tag{2.30}$$

Using this setup, any signal $S(\theta, \phi)$ on the unit sphere can be decomposed into an orthonormal basis of SH coefficients which completely determine the shape of the function. If N samples of this function are taken at $(\theta_i, \phi_i), i = 1, 2, 3, ...N$, then

$$S(\theta_i, \phi_i) = \Sigma_{j=1}^{M} c_j Y_j(\theta_i, \phi_i) \tag{2.31}$$

where $M = (l + 1)(l + 2)/2$ is the number of coefficients in the SH series of order l. Apart from providing a dictionary for sparse representation of the function on the sphere, the utility of using SH basis is that it is an eigenfunction for the Laplace-Beltrami operator. Specifically,

$$\nabla_b^2 Y_l^m = -l(l + 1)Y_l^m \tag{2.32}$$

In case of discrete samples, this can be represented as a simple inverse problem using matrices. If S represents the N samples acquired on the sphere as a column vector, and C represents the column vector of SH coefficients with size $M = (l + 1)(l + 2)/2$, and T represents the NxM matrix of discrete samples on the sphere, then

$$C = (T^T T)^{-1} T^T S \tag{2.33}$$

with which the SH coefficients are derived. Using the Funk-Hecke Theorem, the FRT can be estimated from the SH coefficients, as defined by

$$FRT\{E(\vec{q})\}(\theta, \phi) = \Sigma_j 2\pi \frac{P_{l(j)(0)}}{P_{l(j)(1)}} c_j Y_j(\theta, \phi) \tag{2.34}$$

Combining this result with the previously derived expression for the ODF based on

FRT, the matrix equation to solve for the ODF based on samples of $E(\vec{q})$ is given by

$$ODF \approx \begin{pmatrix} \ddots & & \\ & 2\pi \frac{P_{l(j)(0)}}{P_{l(j)(1)}} & \\ & & \ddots \end{pmatrix} \begin{pmatrix} \vdots \\ c_j \\ \vdots \end{pmatrix} \tag{2.35}$$

where c_j are the SH coefficients for the data using the exponential signal model. With these mathematical simplifications, the ODF calculation becomes a simple linear matrix operation, once the T matrix has been evaluated for the N gradient acquisition directions. The entire process is represented as a block diagram in Fig. 2.7. The SH coefficients for estimating the ODF can be obtained from the result using Eq. 2.35.

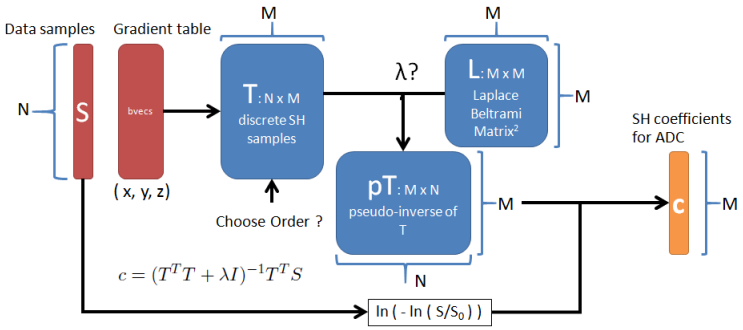

Figure 2.7: A block diagram for SH coefficient estimation with the Laplace-Beltrami regularization.

2.3.3 Anisotropy measures

Shape measures akin to FA are available for ODFs as well. This is aptly called Generalized FA (GFA), and is calculated directly from the SH coefficients of the ODF. The expression for GFA is

$$GFA = \frac{1}{\sqrt{1 + \frac{1}{4\pi \Sigma_{i=2}^{M} c_i^2}}} \tag{2.36}$$

This quantity is similar to FA, ranging from 1 for diffusion along a single direction to 0 for isotropic diffusion. The GFA image is used in all visualizations of the ODF as it provides a good sense of the underlying anatomical structures for further analysis.

2.3.4 Drawbacks

The CSA-ODF model for a single shell is based on a mono-exponential signal decay model. It is known that a bi-exponential signal model is more appropriate for data fitting, and this is exploited in the next section. The ODF that we estimate is generally called the diffusion ODF, which is not the same as the fiber ODF, the probability of there being axonal fibers along a particular direction. Methods for getting around this problem have been proposed using spherical de-convolution [14], model-based methods like the ball-stick model [15], and general compartment based models [16]. The current formulation also fixes the sample directions to follow a certain geometry which has scope for improvements. We discuss the optimization and generalization of this scheme in the next section.

2.4 Generalization of the CSA-ODF Algorithm

The major contributions of this thesis is presented in the following two sections. An extension to the CSA-ODF algorithm to support any q-space acquisition is presented, along with recommendations for the sampling schemes on multiple shells. This is followed by a short description of the bi-exponential model and the interpolation scheme used on each shell.

2.4.1 Multi-shell acquisitions

With more complex diffusion profiles to model, it has become quite clear that a single q-shell acquisition to estimate a mono-exponential radial signal decay model is insufficient. The simplest way to deal with this drawback is to sample the q-space over multiple concentric shells, with data available at more than one value of q along any given $\hat{u}$. With more data points, estimating higher order models becomes feasible. Although this seems to be similar to the DSI acquisition scheme, it is to be noted that the emphasis is still on orientations based on (θ, ϕ) rather than sampling on a 3-D grid. Typically, two or three shells are chosen, based on trade-offs regarding SNR and angular orientation accuracy. In spite of the limitation of choosing a set of shell radii, several different acquisition schemes are possible. These schemes are discusssed in the following section.

2.4.2 Sampling schemes

Our experimental setup makes use of two sampling schemes referred to as 'staggered' and 'aligned'. For the sake of illustration, let the number of q-space points acquired be N, and let us also assume that these are divided equally between three shells. The 'aligned' scheme chooses $N/3$ directions, and samples each shell along the same $N/3$ directions. Consequently, along any acquisition direction $\hat{u}$, we have three data points, at distinct radii defined by the b-values used in the acquisition. Having three points allows more descriptive signal models as elaborated in the following section.

In contrast, the 'staggered' scheme lets the acquisition directions be independent of the shell it is acquired on. In effect, we have N gradient directions, and no direction is sampled more than once. Along any direction $\hat{u}$, there is just one sample acquired, and each shell will have $N/3$ independent points. With assumptions on the signal decay, if an interpolation scheme per-shell is utilized, it becomes redundant to actually acquire the signal at different b-values. For the same acquisition time, the number of samples acquired is now threefold, resulting in better angular resolution of the ODF. This is shown in Figure 2.8.

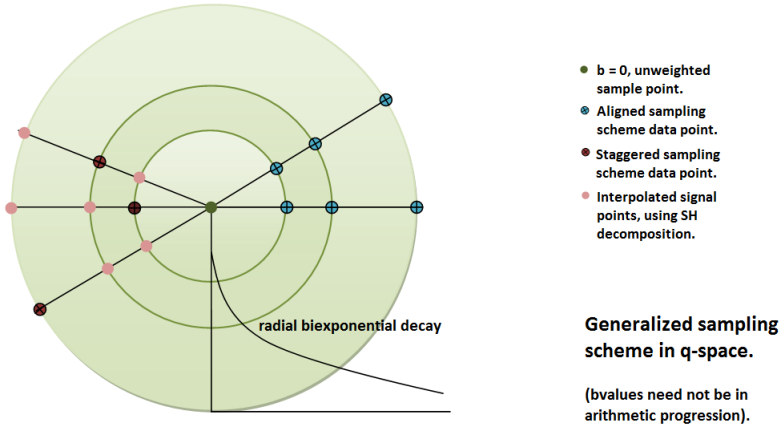

Figure 2.8: Difference between staggered and aligned sampling

2.4.3 Signal Interpolation scheme

SH decomposition of the signal in q-space is used to estimate a continuous function on each shell independently. From Eq. 2.31 it is known that any function can be decomposed into SH coefficients via a lossy-compression process. With the SH coefficients based on the sampled points known, the signal value at any (θ, ϕ) can be estimated using Eq. 2.31.

2.4.4 Bi-exponential signal model

With the q-space signal known on more than one shell, models that fit the data better are utilized. It is known that the bi-exponential radial signal decay model represents the data better, and three shell acquisitions are sufficient to estimate three unknowns in the equation

$$E(q\hat{u}) \approx (\alpha)e^{-\delta^{(1)}q^2} + (1-\alpha)e^{-\delta^{(2)}q^2} \tag{2.37}$$

where α is called the volume fraction of the component with a decay rate $\delta^{(1)}$ and $(1-\alpha)$ will be the fraction for the rest of the volume, with a decay rate $\delta^{(2)}$.

2.5 Regularization

This formulation relies on accurate estimation of the SH coefficients of the log-transformed signal. The calculation for these SH coefficients involves the calculation of the pseudo-inverse of the matrix T of discrete SH samples along the sampled points. Acquisition schemes are designed to let this system be overdetermined, that the number of equations is greater than the number of unknowns. Due to low SNR levels in the signal, regularization schemes are employed to generalize the results well and avoid overfitting the data. Historically, ridge-regression has been applied successfully to such systems of equations. Another popular regularization scheme is the Laplace-Beltrami regularizer. This utilizes the geometry of the problem to define a new minimization objective based on promoting smoothness of the estimated function.

2.5.1 Need for a regularized inverse

Methods to estimate the optimal value for λ have been discussed in [9, 17, 18]. An intuitive understanding for the effects of regularization can be observed using eigen-decomposition of the T matrix. For underdetermined systems, there exist eigenvalues which evaluate to 0, leading to the non-existence of an inverse. In case of over-determined systems, in case of sparse representations, the ratio of the largest eigenvalue to the smallest (called the condition number for the matrix) is of the order 10^{20} and larger. When the smaller eigenvalue constituents are subject to noisy samples for estimation, even small variations in noise lead to large variations in the SH coefficient estimates. This happens specifically due to the inversion of these small eigenvalues. To avoid this, regularized inverses are common. The regularization term creates an artificial filtering effect, giving higher weights to larger eigenvalue components as compared to the smaller eigenvalue components, effectively damping out the effect of noisy samples. This is known to generalize well to noisy data. Regularized inversion is parameterized by λ which ideally is between the highest and lowest singular value of T.

The first step of the generalized CSA-ODF algorithm creates a continuous representation of the diffusion signal on each shell. To that end, we fit SH series of order 4, 6 or 8. The regularized least squares solution for the inverse problem of estimating the SH coefficients is given by:

$$c = (T^T T + \lambda I)^{-1} T^T S \tag{2.38}$$

where c is the vector of SH coefficients, S is the normalized signal, I is the identity matrix, and λ is the regularization parameter.

2.5.2 Tikhonov regularization

This is the standard formulation for ridge-regression, useed in the context of ODF estimation by Hess et al. [19]. λ parameterizes the level of smoothing, and larger values smooth more. Typically, λ has to be in between the largest and smallest eigenvalues of

T for effective smoothing. The choice of λ defines the filter-factor,

$$f_i \approx \frac{\sigma_i^2}{\sigma_i^2 + \lambda^2} \approx \begin{cases} 1, & \text{if } \sigma_i >> \lambda \\ \frac{\sigma_i^2}{\lambda^2}, & \text{if } \sigma_i << \lambda \end{cases} \tag{2.39}$$

These f_i, for each of the i eigenvalues of the system filter the corresponding components such that small eigenvalues of T are given lower weights as part of the inverse. Specifically, the T matrix has rows equal to the number of samples acquired on the shell, and columns equal to the number of SH coefficients to be estimated. The pseudo-inverse of T will be composed of the eigenvalues scaled by the filter-factors.

2.5.3 Laplace-Beltrami regularization

Laplace-Beltrami regularization has been extensively used in the context of ODF reconstruction mostly because of the simple form of the Laplace-Beltrami operator for functions described by SH series [9]. It is controlled by replacing the identity matrix in Equation (2.38) by L (the square of the Laplace-Beltrami matrix) whose diagonal elements are $(l+1)^2 l^2$, where l is the order of the SH at the corresponding column. This is preferred to the standard ridge-regression formulation due to the additional shape parameters it includes, which leads to smoother estimates of the SH coefficients.

2.5.4 Calculation of λ based on acquisition parameters

λ needs to be adjusted as a function of the acquisition and reconstruction parameters. We carried out an exhaustive investigation of the optimal choice of regularization for eleven b-values in the range $[1000, 1500, ...6000] s/mm^2$, five SNR=$5, 15, 25, 35$, and 45, three SH reconstruction orders of 4, 6 and 8, and finally, three fiber configurations with 1, 2 or 3 orientations. The optimal λ value is calculated using the GCV method [18], rather than the L-curve method, since the L-curve method assumes the discrete Piccard conditions [17], which is not true for Equation (2.38).

Fig. 2.9 and Fig. 2.10 shows surface plots of λ, for varying b-values and SNRs. Two SH orders are represented in the case of a two-fiber configuration. Each data point is obtained as the average optimal λ for 100 repetitions with randomly selected angles between fibers. Table 2.5.4 provides numerical values in the three-fiber case. The trends show that lesser regularization is necessary for higher SNRs, and that the optimal λ can

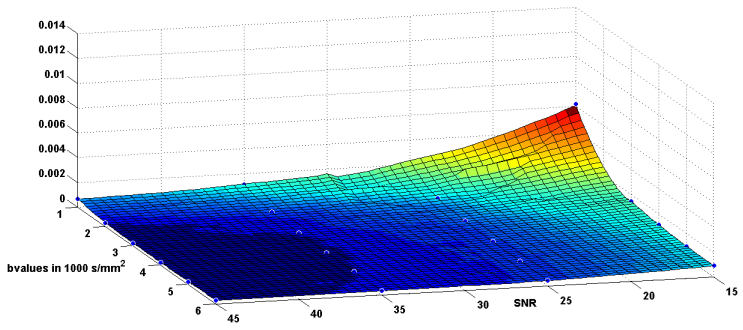

Figure 2.9: Surface plot of lambda for order 4 for the two-fiber configuration as a function of SNR and b-value.

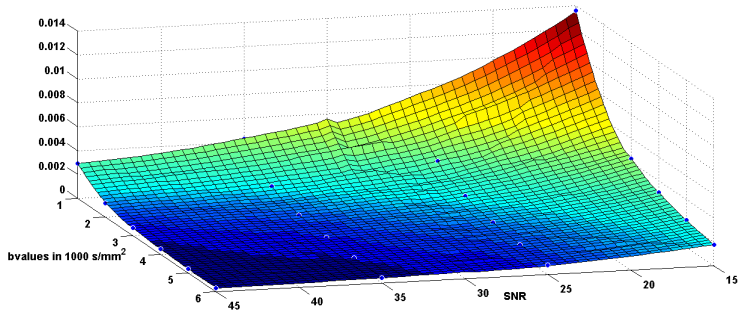

Figure 2.10: Surface plot of lambda for order 6 for the two-fiber configuration as a function of SNR and b-value.

deviate quite significantly from the commonly used 0.006 value , especially at SNR=25 and b-values greater than $1500 s/mm^2$. Interestingly, at all orders, regularization slightly decreases with increased b-value for a given SNR. This behavior is consistent across the three investigated configurations.

Eight other tables similar to Table 2.5.4 are available, therefore making it possible to adjust the choice of λ to specific experimental conditions. This regularization scheme is applied for the interpolation stage, where the SH coefficient are estimated from noisy samples in q-space. It is not used for the calculation of the ODF as smoothing of the signal is not necessary at that stage.

b-value	SNR: 5	SNR: 15	SNR: 25	SNR: 35	SNR: 45
1000	0.083302	0.014496	0.011214	0.006020	0.004279
1500	0.038631	0.008837	0.004006	0.001763	0.002086
2000	0.047775	0.006534	0.002520	0.001391	0.001055
2500	0.017271	0.004824	0.001556	0.000823	0.000573
3000	0.021266	0.002089	0.001388	0.000670	0.000429
3500	0.026	0.002072	0.001057	0.000470	0.000318
4000	0.027045	0.001593	0.0006	0.00037	0.000319
4500	0.01063	0.002516	0.000865	0.000676	0.000243
5000	0.024093	0.001576	0.000795	0.000448	0.000453
5500	0.022867	0.001241	0.000788	0.000383	0.000391
6000	0.020809	0.001715	0.001317	0.000419	0.000353

Table 2.1: Optimal λ values for three-fiber, order 6 reconstruction (b-value in s/mm^2).

Chapter 3

Results

3.1 Synthetic data

We make use of realistic diffusion models available in Camino [20], a diffusion MRI toolkit developed at UCL, UK. Panagiotaki et al. [21] have documented an extensive collection of diffusion data models in their paper, and we use the compartment models to carry out the simulation studies. We use three compartments for single-fiber configurations and five compartments for two-fiber configurations, with volume fractions 0.6 for the intra-axonal, 0.1 for the extra-axonal, and 0.3 for the isotropic compartment. This is scaled as 0.3 for each intra-axonal, 0.05 for each extra-axonal and 0.3 for isotropic compartments in the two-fiber case. The intra-axonal compartment is modeled as a cylinder of radius $0.004mm$ with a gaussian phase distribution (GPD) and diffusivity $0.0017mm^2/s$. The extra-axonal compartment is modeled as a zeppelin with diffusivity $0.0017mm^2/s$ along the fiber, and $0.0002mm^2/s$ across it. The isotropic component is modeled as a dot. Eleven b-values: $[1000, 1500, 2000, ...6000]s/mm^2$ are calculated using the following pulse sequence parameters G = 0.05 T/m, TE = $0.1s$, $\delta = 0.02s$ and varying Δ.

In order to illustrate the performance of the bi-exponential model fit, we provide in Fig. 3.1 the signal decay profile as a function of b-values along various directions for a single- and two-fiber configurations. The cylinder-dot-zeppelin compartment model [21] was used to generate data at SNR 15, along 300 directions.

We set a maximum number of 300 gradient directions divided across three shells

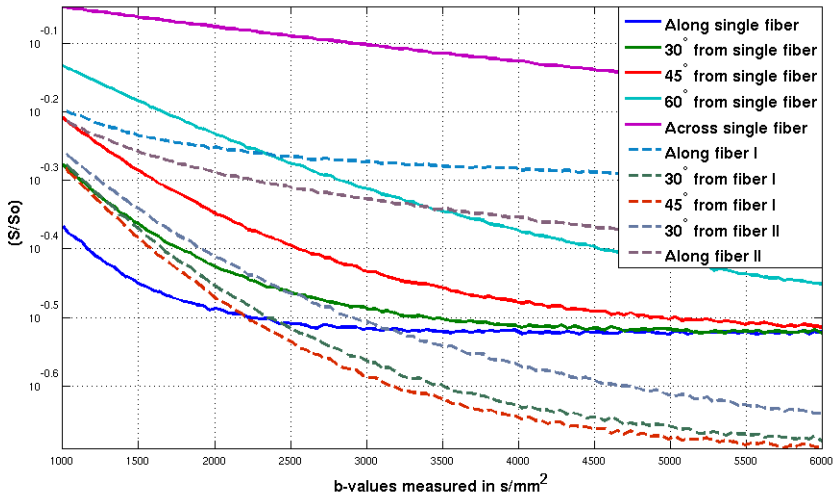

Figure 3.1: Bi-exponential decay for the single- and two-fiber configurations.

as the basis for sampling the q-space. For ground truth signal and associated ODF, we choose the same 300 directions on eleven shells (from the 11 b-values), at SNR 40. The L^2 norm of the difference in the SH coefficients and the symmetrized Kullback Liebler Divergence (KL) is used as a measure of similarity of ODFs, so that accuracy of reconstruction can be quantified.

3.2 Optimal b-value analysis

We study the effects of varying the sets of b-values to accurately estimate the ODF. We restrict ourselves to fourteen representative sets of three b-values. We will demonstrate in the following that adding a fourth shell only improve performance marginally. We restrict the range up to a b-value of $6000 s/mm^2$ as most of the bi-exponential nature of the diffusion signal is concentrated in the range of $1500 - 4000 s/mm^2$. We fix the total number of gradient directions to 300 (distributed as 21, 86, 193 over the shells). All SNRs, single- and two-fiber configurations and SH orders 4 and 6 are tested. The corresponding optimal λ is always chosen from Section 2.5. In each case, as for all experiments from now on, 20 repetitions are performed and the mean result reported. Results of this simulation are shown in Fig. 3.2. The set $[1000, 2000, 6000] s/mm^2$ shows

lower error at SNR=15, 25 or 40 for an order 4 reconstruction and one-fiber configuration. Similar trends are observed at SNR 5 although, as expected, with much higher reconstruction error levels. Results are consistent with Fig. 3.1, where the signal decay exhibits the highest deviation from the mono-exponential behavior in the vicinity of b-value $2000 s/mm^2$. b-value sets that skip this critical region show errors that are considerably larger as they do not capture the bi-exponential nature of the diffusion signal. b-value sets $[1000, 2000, 3000/4000/5000] s/mm^2$ exhibit similar performance but we focus on the set $[1000, 2000, 6000] s/mm^2$ to demonstrate the performance of the bi-exponential fitting algorithm in the most non-uniform sampling case.

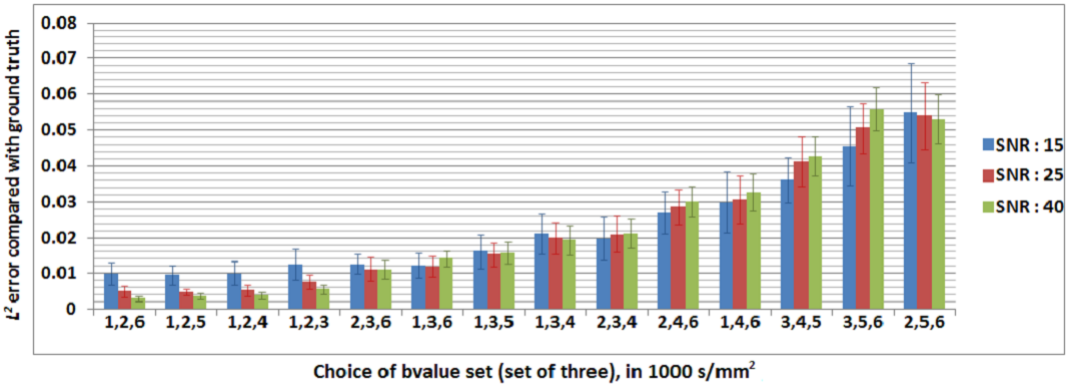

Figure 3.2: Error chart for different sets of b-value in the 3-shell case.

b-value $[1000, 2000, 6000]$ s/mm^2 show superior reconstruction in all our tests as seen in Fig. 3.3. Clearly, b-value sets including 1000 and $2000 s/mm^2$ and with $3000, 4000, 5000$ or $6000 s/mm^2$ as third shell outperform other combinations. We will consider $[1000, 3000, 5000]$ and $[1000, 4000, 6000] s/mm^2$ respectively as "average" and "poor" candidates for subsequent comparisons.

3.3 Optimal gradient table analysis

Reconstruction error is studied for a reduced number of total points, with all the other parameters remaining unchanged. This provides a quantitative measure of the loss in reconstruction accuracy, in comparison with the ground truth. Fig. 3.4 (for a two-fiber configuration at SNR 25) shows how the error decreases as the number of sample

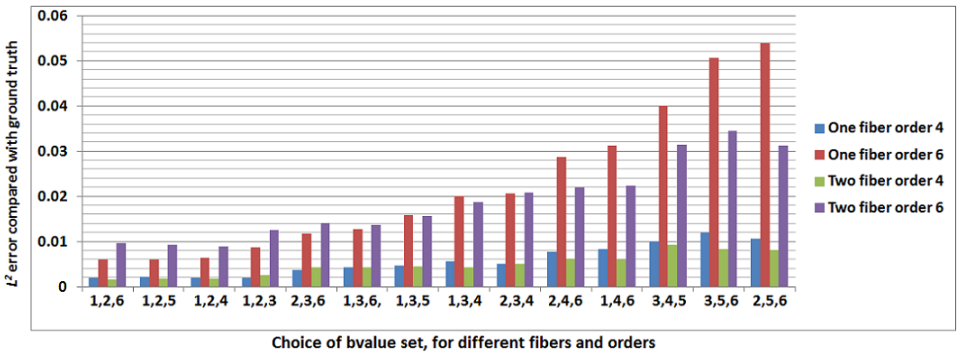

Figure 3.3: Average reconstruction error for four combinations of SH order and fibers.

points increases. It is seen that the curves are nearly flat after around 200 directions. Moreover, b-value sets previously identified as "good", "average" and "poor" preserve their relative performance with increasing number of directions.

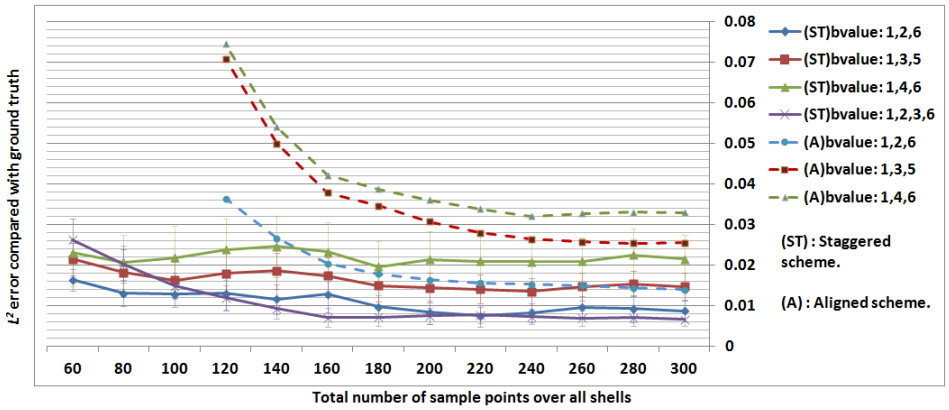

Figure 3.4: Reconstruction error as a function of the number of directions acquired for different cases of b-value for two-fiber configuration at SNR 25, order 6 reconstruction.

Additionally, we compare the *aligned* sampling scheme with the *staggered* scheme for the same total number of data points over all shells, e.g: 300 *staggered* points divided as 21,86 and 193 are compared with 300 *aligned* points divided as 100, 100 and 100. Fig. 3.4 shows the reconstruction errors in both cases. The interpolation step in the *staggered* case does not introduce significant distortions. Moreover, this approach clearly provides a better angular resolution and improves ODF reconstruction. Fig. 3.4 also shows that a four-shell $[1000, 2000, 3000, 6000]s/mm^2$ acquisition does not provide an appreciable

increase in accuracy. It therefore illustrates that three points are likely sufficient to estimate the three parameters α, $\delta^{(1)}$ and $\delta^{(2)}$.

3.4 Angular accuracy

We investigate the minimum achievable separating angle between fiber orientations using the *staggered* acquisition scheme with 200 directions, b-values of $[1000, 2000, 6000] s/mm^2$, SH order 8 and SNR 40. It has been demonstrated that angles around 30 degrees can be recovered when using order 8 SH series.

Fig. 3.5 shows the reconstruction in steps of 10 degrees from orthogonal to a single-fiber configuration, with an order 8 reconstruction. The * indicates the minimum angle between which we resolve crossings, which precisely happens between 35 and 30 degrees.

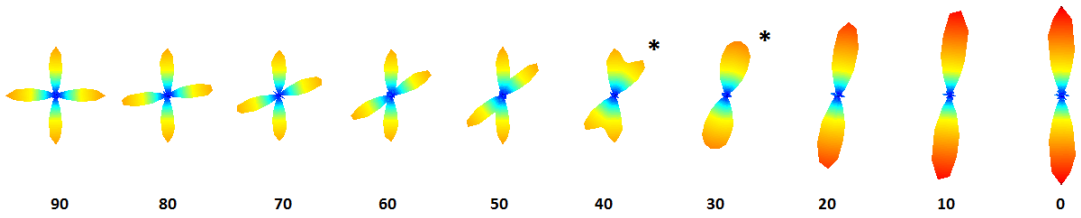

Figure 3.5: Angular resolution in the two-fiber case, varying from orthogonal-fiber to a single-fiber configuration.

mean ± std	SNR: 5	SNR: 15	SNR: 25	SNR: 40
Order: 4	5.3759 ± 2.0902	1.5826 ± 0.6079	1.0886 ± 0.4610	0.7299 ± 0.2736
Order: 6	5.4046 ± 2.1040	1.5992 ± 0.6564	1.1093 ± 0.4642	0.7463 ± 0.2725
Order: 8	5.4309 ± 2.1006	1.6184 ± 0.6215	1.0920 ± 0.4685	0.7356 ± 0.2769

Table 3.1: Angular error performance (degrees) for an orthogonal-fiber configuration.

Table 3.4 summarizes the angular error achieved with the same sampling scheme but varying SH orders and SNR for an orthogonal two-fiber configuration. For each case, 100 repetitions were performed and the mean ± standard deviation of the angular error between the estimated ODF maxima and the true orientation are reported. Even at low SNR, the maximum error is around 5 degrees. For realistic SNR, an average error of 1 degree is achieved which outperforms many existing ODF reconstruction technique.

3.5 Validation on Human Brain Data

Finally, our generalized CSA-ODF algorithm was applied to human brain data from a healthy volunteer, acquired on a 3T Siemens scanner with the following parameters: Voxel size $1.5mm$ isotropic, TR/TE=3200/77ms, 133 aligned DWI at b= $[1000, 2000, 3000]s/mm^2$ and 10 $b0$. ODF reconstructions are presented in Fig. 3.6. Fiber crossings in the centrum semiovale and various other complex white matter areas are successfully recovered. Moreover, we down-sampled the data by half (from 133 to 67 directions) and verified (Fig. 3.6) that the ODF reconstruction still performed very well. This is expected from our simulations, although a staggered scheme was not available for this dataset (in which case we would expect even better results).

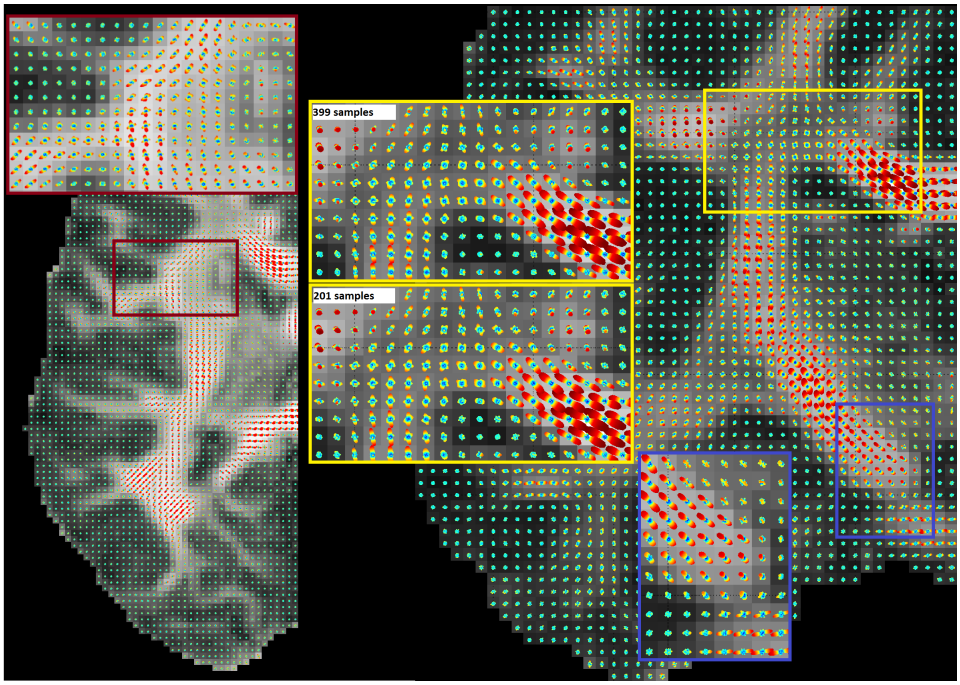

Figure 3.6: The generalized CSA-ODF algorithm applied to brain data, superimposed on a Generalized Fractional Anisotropy (GFA) map with an aligned sampling scheme.

Chapter 4

Conclusion

This thesis deals with the generalization of the CSA-ODF model to account for a flexible acquisition scheme, and provides an analysis of the optimal parameters for the reconstruction of the ODF. It is observed that specific sets of b-values (e.g. $[1000, 2000, 6000]$ s/mm^2) perform clearly better, which can be explained by looking deeper into the bi-exponential nature of the diffusion signal decay. For this particular reconstruction algorithm, three-shell acquisitions perform nearly as well as four-shell acquisitions, and around 200 gradient directions are sufficient for good angular resolution as well as accuracy.

With this analysis, it is hoped that acquisitions for the Human Connectome Project would be tuned for the collection of the best dataset. It is also hoped that this study would prove to be a template for further studies in optimizing acquisition schemes for Diffusion MR imaging.

References

[1] K. K. Seunarine and D. C. Alexander. Chapter 4 - multiple fibers: Beyond the diffusion tensor. In *Diffusion MRI*, pages 55 – 72. Academic Press, 2009.

[2] D.C. Alexander. An introduction to computational diffusion MRI: the diffusion tensor and beyond. *Visualization and processing of tensor fields*, pages 83–106, 2006.

[3] J.P. Hornack. The basics of MRI: `http://www.cis.rit.edu/htbooks/mri/`, September 2012.

[4] V.S.Ramachandran. *Phantoms in the Brain*. William Morror, 1998.

[5] The human brain - Wikipedia: `http://en.wikipedia.org/wiki/Human_brain`, September 2012.

[6] S. Seung. *I am my Connectome*. Houghton Mifflin Harcourt Trade, 2012.

[7] P. J. Basser, J. Mattiello, and D. L. Bihan. MR diffusion tensor spectroscopy and imaging. *Biophysical Journal*, 66:259–267, 1994.

[8] D. S. Tuch. Q-ball imaging. *Magn. Reson. Med.*, 52(6):1358–1372, 2004.

[9] M. Descoteaux, E. Angelino, S. Fitzgibbons, and R. Deriche. Regularized, fast, and robust analytical q-ball imaging. *Magn. Reson. Med.*, 58(3):497–510, 2007.

[10] I. Aganj, C. Lenglet, G. Sapiro, E. Yacoub, K. Ugurbil, and N. Harel. Reconstruction of the orientation distribution function in single-and multiple-shell q-ball imaging within constant solid angle. *Magn. Reson. Med.*, 64(2):554–566, 2010.

[11] E. O. Stejskal and J. E. Tanner. Spin diffusion measurements: Spin echoes in the presence of a time-dependent field gradient. *The Journal of Chemical Physics*, 42(1):288–292, 1965.

[12] Y. Assaf and Y. Cohen. Chapter 7 - inferring microstructural information of white matter from diffusion MRI. In *Diffusion MRI*, pages 127 – 146. 2009.

[13] V. J. Wedeen, P. Hagmann, W.-Y. I. Tseng, T. G. Reese, and R. M. Weisskoff. Mapping complex tissue architecture with diffusion spectrum magnetic resonance imaging. *Magn. Reson. Med.*, 54(6):1377–1386, 2005.

[14] J.-D. Tournier, C.-H. Yeh, F. Calamante, K.-H. Cho, A. Connelly, and C.-P. Lin. Resolving crossing fibres using constrained spherical deconvolution: Validation using diffusion-weighted imaging phantom data. *NeuroImage*, 42(2):617 – 625, 2008.

[15] T. E. J. Behrens, M. W. Woolrich, M. Jenkinson, H. Johansen-Berg, R. G. Nunes, S. Clare, P. M. Matthews, J. M. Brady, and S. M. Smith. Characterization and propagation of uncertainty in diffusion-weighted MR imaging. *Magn. Reson. Med.*, 50(5):1077–1088, 2003.

[16] S. Jbabdi, S. N. Sotiropoulos, A. M. Savio, M. Grana, and T. E. J. Behrens. Model-based analysis of multishell diffusion MR data for tractography: How to get over fitting problems. *Magnetic Resonance in Medicine*, 2012.

[17] P. C. Hansen. Analysis of discrete ill-posed problems by means of the L-curve. *SIAM Review*, 34(4):pp. 561–580, 1992.

[18] G. H. Golub, M. Heath, and G. Wahba. Generalized cross-validation as a method for choosing a good ridge parameter. *Technometrics*, 21(2):pp. 215–223, 1979.

[19] C. P. Hess, P. Mukherjee, E. T. Han, D. Xu, and D. B. Vigneron. Q-ball reconstruction of multimodal fiber orientations using the spherical harmonic basis. *Magn. Reson. Med.*, 56(1):104–117, 2006.

[20] P.A. Cook, Y. Bai, S. Nedjati-Gilani, K. K. Seunarine, M. G. Hall, G. J. Parker, and D.C. Alexander. Camino: Open-source diffusion-MRI reconstruction and processing. *14th scientific meeting of the ISMRM*, 2759, 2006.

[21] E. Panagiotaki, T. Schneider, B. Siow, M. G. Hall, M. F. Lythgoe, and D. C. Alexander. Compartment models of the diffusion MR signal in brain white matter: A taxonomy and comparison. *NeuroImage*, 59(3):2241 – 2254, 2012.

‘